Dynamics of Cas10 Govern Discrimination between Self and Non-self in Type III CRISPR-Cas Immunity

Graphical Abstract

Highlights

- Self RNA locks Cas10 in a static inactive configuration, thus avoiding autoimmunity

- Non-self RNA triggers fast conformational fluctuations within Cas10 and activates it

- Target mismatches differentially modulate the conformational dynamics of Cas10

- Internal flexibility of the effector complex enables tunable CRISPR immune response

Authors

Ling Wang, Charlie Y. Mo, Michael R. Wasserman, Jakob T. Rostøl, Luciano A. Marraffini, Shixin Liu

Correspondence

shixinliu@rockefeller.edu

In Brief

Type III CRISPR-Cas systems employ an RNA-DNA dual-targeting mechanism to eliminate invading pathogens. Using single-molecule fluorescence spectroscopy, Wang et al. show that the conformational dynamics of Cas10—the signature subunit of type III effector complexes—control the discrimination between self and non-self elements and the strength of CRISPR immunity.

CellPress

Dynamics of Cas10 Govern Discrimination between Self and Non-self in Type III CRISPR-Cas Immunity

Ling Wang,[1] Charlie Y. Mo,[2] Michael R. Wasserman,[1] Jakob T. Rostøl,[2] Luciano A. Marraffini,[2] and Shixin Liu[1,3,*]
[1]Laboratory of Nanoscale Biophysics and Biochemistry, The Rockefeller University, 1230 York Avenue, New York, NY 10065, USA
[2]Laboratory of Bacteriology, The Rockefeller University, 1230 York Avenue, New York, NY 10065, USA
[3]Lead Contact
*Correspondence: shixinliu@rockefeller.edu
https://doi.org/10.1016/j.molcel.2018.11.008

SUMMARY

Adaptive immune systems must accurately distinguish between self and non-self in order to defend against invading pathogens while avoiding autoimmunity. Type III CRISPR-Cas systems employ guide RNA to recognize complementary RNA targets, which triggers the degradation of both the invader's transcripts and their template DNA. These systems can broadly eliminate foreign targets with multiple mutations but circumvent damage to the host genome. To explore the molecular basis for these features, we use single-molecule fluorescence microscopy to study the interaction between a type III-A ribonucleoprotein complex and various RNA substrates. We find that Cas10—the DNase effector of the complex—displays rapid conformational fluctuations on foreign RNA targets, but is locked in a static configuration on self RNA. Target mutations differentially modulate Cas10 dynamics and tune the CRISPR interference activity *in vivo*. These findings highlight the central role of the internal dynamics of CRISPR-Cas complexes in self versus non-self discrimination and target specificity.

INTRODUCTION

A fundamental attribute of immune systems is their ability to distinguish foreign from self elements, which is imperative for the host to eliminate invading pathogens while avoiding autoimmunity (Boehm, 2006). Clustered regularly interspaced short palindromic repeats (CRISPR) loci and CRISPR-associated (*cas*) genes represent an adaptive immune mechanism for prokaryotes to defend against phage and plasmid infection (Barrangou et al., 2007; Marraffini and Sontheimer, 2008). In this mechanism, fragments of the invading DNA are inserted between CRISPR repeats in the host genome. The inserts, known as spacers, are subsequently transcribed and processed into CRISPR RNA (crRNA), which assemble with a specific set of Cas proteins to form ribonucleoprotein effector complexes.

Upon re-infection, immunity is conferred by crRNA-guided recognition and degradation of the invading genetic element by the effector complex.

Based on their *cas* gene content, CRISPR-Cas systems can be classified into six major types (I–VI) (Koonin et al., 2017). Type III systems, which are identified by their signature *cas10* gene, are further divided into subtypes: III-A/D, which encodes the Cas10-Csm complex, and III-B/C, which encodes the Cas10-Cmr complex. Type III effector complexes employ a uniquely elaborate targeting mechanism (Pyenson and Marraffini, 2017; Tamulaitis et al., 2017) in which active transcription of the target sequence is required for CRISPR immunity (Deng et al., 2013; Goldberg et al., 2014). crRNA derived from the spacer-repeat array guides the Cas10-Csm/Cmr complex to transcribed target RNA containing a protospacer sequence complementary to the crRNA spacer. Multiple copies of the Csm3/Cmr4 subunit in the complex—harboring crRNA-guided RNase activity—cleave the target RNA in 6-nucleotide (nt) intervals (Hale et al., 2009; Samai et al., 2015; Staals et al., 2013; Tamulaitis et al., 2014; Zhang et al., 2012). Binding of the complex to the target RNA further triggers single-stranded DNA (ssDNA) degradation, which is carried out by the Cas10 subunit (Elmore et al., 2016; Estrella et al., 2016; Kazlauskiene et al., 2016). Besides the DNase activity, Cas10 also harbors the catalytic activity to convert ATP into cyclic oligoadenylates (cOA) (Kazlauskiene et al., 2017; Niewoehner et al., 2017). This signaling molecule activates Csm6—another RNase encoded by the type III-A loci—for non-specific RNA degradation, which becomes essential for immunity when the target is located in late-expressed genes or contains mismatches to the spacer (Jiang et al., 2016).

Such an RNA-DNA dual-targeting mechanism contrasts with the one employed by type I and II systems, which generally target double-stranded DNA (dsDNA). Moreover, type III systems adopt a distinctive mechanism for self versus non-self discrimination. To specify a target, type I and II systems recognize short (2–4 nt) protospacer adjacent motifs (PAMs), which are present in the invading DNA but absent from the host's own CRISPR repeats (Gasiunas et al., 2012; Mojica et al., 2009). By contrast, type III systems rely on the crRNA "tag," an 8-nt sequence derived from the CRISPR repeat located at the 5′ flank of mature crRNA. Non-complementarity between the crRNA tag and the 3′ flanking sequence of the protospacer licenses a foreign target and triggers an immune response,

whereas complementarity specifies host genetic elements and prevents self targeting (Marraffini and Sontheimer, 2010). Notably, homology between the crRNA tag and the 3′-flanking target sequence does not affect RNA cleavage, but rather inhibits ssDNA cleavage by Cas10 (Kazlauskiene et al., 2016; Samai et al., 2015). However, the molecular mechanism by which Cas10's DNase activity is switched on or off by the 3′-flanking sequence remains unknown.

Compared to other CRISPR types, type III systems also display an unusually high level of tolerance to mutations in the protospacer sequence (Goldberg et al., 2014; Kazlauskiene et al., 2016; Manica et al., 2013; Maniv et al., 2016; Peng et al., 2015; Staals et al., 2014). A recent comprehensive mutational survey confirmed the broad target specificity and further showed that the accumulation of mutations may weaken, but not abrogate, the immune response to varying degrees depending on the position of the mutations in the protospacer (Pyenson et al., 2017). Nonetheless, how the strength of immunity is differentially modulated by target mutations is still poorly understood.

Single-molecule techniques are powerful tools for dissecting dynamic protein-nucleic acid interactions and have been employed to study types I, II, and V CRISPR-Cas systems (Blosser et al., 2015; Chen et al., 2017; Dagdas et al., 2017; Dillard et al., 2018; Jeon et al., 2018; Lim et al., 2016; Loeff et al., 2018; Osuka et al., 2018; Redding et al., 2015; Rutkauskas et al., 2015; Singh et al., 2016, 2018; Sternberg et al., 2014; Szczelkun et al., 2014; Xue et al., 2017; Yang et al., 2018). Here, we used single-molecule fluorescence microscopy to investigate the targeting mechanism of a type III-A Cas10-Csm complex. We found that Cas10 displays strikingly distinct behaviors on self versus non-self RNA: it is locked in a static configuration on host CRISPR transcripts, but samples a large conformational space upon binding to foreign RNA. Among the many states explored by Cas10 on target RNA, a subset is enriched by the presence of ssDNA or ATP and is sensitively modulated by mutations in the protospacer region of the target. The occupancy of Cas10 at these states is predictive of the CRISPR interference efficiency measured *in vivo*, suggesting that they correspond to the active configuration of the effector complex. These results highlight the exquisite allosteric regulation of the conformational fluctuations of the effector complex by the target sequence and provide the molecular basis for self versus non-self discrimination and mutation tolerance in type III CRISPR-Cas immunity.

RESULTS

Single-Molecule Fluorescence Platform for Studying Type III CRISPR-Cas Immunity

We chose the type III-A CRISPR-Cas system from *Staphylococcus epidermidis* as our model system. Its CRISPR loci encode for a Cas10-Csm complex composed of Cas10($\times$ 1), Csm2($\times$ 3), Csm3($\times$ 5), Csm4($\times$ 1), Csm5($\times$ 1), and a crRNA. We used an engineered *S. epidermidis* CRISPR-Cas locus that contains one single spacer targeting the capsid gene *gp43* of the staphylococcal lytic phage ΦNM1γ6 (Figure S1; Jiang et al., 2016). Cas10-Csm complexes harboring mature crRNA were heterologously expressed in *Escherichia coli*. For single-molecule experiments, RNA substrates were labeled with a biotin and a Cy3 fluorophore

at opposite ends. Individual RNA molecules were immobilized on a glass coverslip, and their fluorescence signals were detected by total-internal-reflection fluorescence microscopy. RNA cleavage by the Cas10-Csm complex would result in release of the fluorophore into the solution and, thus, a decrease in the surface density of Cy3 fluorescent spots (Figure 1A). Three types of RNA substrates were assessed (Figure 1B): (1) a wild-type ("WT") RNA—mimicking bona fide RNA targets—that contains a 35-nt protospacer sequence complementary to the crRNA spacer and a 3′-flanking sequence that is non-complementary to the crRNA 5′ tag; (2) an "anti-tag" RNA—mimicking RNA molecules generated by antisense transcription of the host's own CRISPR array—that contains both a matching protospacer sequence and an 8-nt 3′-flanking anti-tag sequence; and (3) a "non-specific" RNA containing a scrambled sequence with no homology to the crRNA. In the presence of Mg^{2+}, the surface density of WT and anti-tag RNAs decreased at similar rates, demonstrating that these two substrates were both efficiently cleaved by Csm3 (Figures 1C and 1D). The rate obtained from the single-molecule assay was comparable to that measured in bulk (Figure 1D). In contrast, minimal cleavage was observed with the non-specific RNA or in the absence of Mg^{2+} (Figures 1D and S2A). These results are consistent with previous studies showing that base pairing with the crRNA tag, as is the case for the anti-tag RNA, does not inhibit the RNA cleavage activity of the effector complex (Samai et al., 2015; Tamulaitis et al., 2014). It is noteworthy that RNA cleavage products are quickly released by the complex—as reflected by the disappearance of fluorescent spots from the surface—unlike Cas9-mediated DNA targeting, in which DNA remains stably bound to the complex even after cleavage (Sternberg et al., 2014). This feature ensures a tight temporal control of the ssDNA degradation and cOA synthesis activities of Cas10, which rely on target RNA engagement (Kazlauskiene et al., 2016; Rouillon et al., 2018). It also potentially allows the type III effector complex to process multiple targets within a short time window.

Dynamic Interaction between the Cas10-Csm Complex and Its RNA Target

Since both self and non-self RNAs can be equally recognized by type III CRISPR complexes for cleavage, we postulated that self versus non-self discrimination might be manifested in distinct binding configurations of the Cas10-Csm complex on different RNA targets. To test this hypothesis, we used single-molecule fluorescence resonance energy transfer (FRET) to probe the interactions between Cas10-Csm and various RNA substrates. We began by focusing on the WT RNA, which mimics transcripts of foreign elements. We designed several FRET labeling schemes based on the structural model for the target-bound Cas10-Csm complex (Kazlauskiene et al., 2016; Osawa et al., 2015; Tamulaitis et al., 2017; Taylor et al., 2015; Figures S1B, S1C, and S2B). First, we attached the FRET donor (Cy3) to the 5′ end of the WT RNA and the FRET acceptor (AlexaFluor647) to the Csm5 subunit, which is located at the distal side of the crRNA tag and Cas10 (Figure 2A). Single-molecule data were collected in an EDTA-containing buffer in order to prevent RNA degradation. Binding of Csm5-labeled Cas10-Csm complexes to 5′-end-labeled WT RNA resulted in a stable FRET state in the vast majority of single-molecule trajectories (93%; Figure 2A).
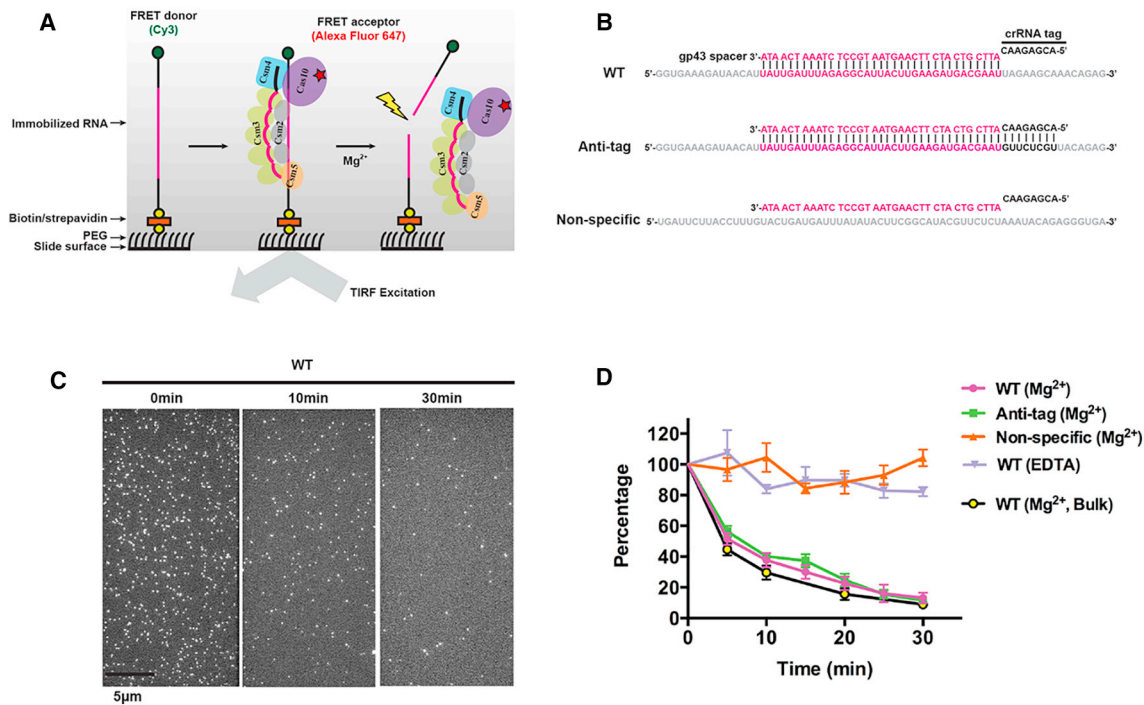
Figure 1. A Single-Molecule Fluorescence Platform for Studying Type III CRISPR-Cas Targeting Mechanism
(A) Schematic of the single-molecule imaging platform.
(B) Sequences of the WT, anti-tag, and non-specific RNAs.
(C) Representative fields of view on a total-internal-reflection fluorescence microscope showing surface-immobilized Cy3-labeled RNA. Disappearance of the fluorescent spots after Mg^{2+} addition reflects the cleavage and release of individual RNA molecules.
(D) Cleavage kinetics for different RNA substrates plotted as the average surface density of molecules against time after Mg^{2+} addition. The surface density of WT RNA remained unchanged when an EDTA-containing buffer without Mg^{2+} was added (purple triangles). The WT RNA cleavage kinetics measured from a bulk assay is shown in yellow circles.
Data are represented as mean ± SD from multiple fields of view (n > 10) for the single-molecule assay or three replicates for the bulk assay.
See also Figures S1 and S2.

The distribution of FRET efficiency (*E*) built from many molecules displayed a single peak centered at ∼0.25 (Figure 2B). This result suggests that the Cas10-distal end of the target-bound complex is largely static.

We then moved the FRET pair to the Cas10-proximal end of the complex, with the donor attached to the 3′ end of the WT RNA and the acceptor labeled on the Csm4 subunit, which makes contacts with the crRNA tag (Figures S1B and S1C). Again we observed one predominant FRET state (*E* ∼0.23) (91% of the trajectories are static; Figures 2C and 2D), suggesting that the 3′-flanking region of the WT RNA, even though unable to base pair with the crRNA tag, is nonetheless stationary relative to Csm4.

We then placed the acceptor fluorophore at the N terminus of Cas10, the largest subunit in the complex and the signature protein of all type III systems (Figures S1B and S1C). In contrast to the previous two labeling schemes, most of the FRET trajectories (80%) obtained with Cas10-labeled complexes and 3′-end-labeled WT RNA were highly dynamic, rapidly sampling many different states (Figures 2E and S3A). Accordingly, we observed a broad FRET distribution, with *E* spanning from 0.1 to 0.8 (Figure 2F). This finding reveals that Cas10 is highly mobile with respect to the rest of the complex.

To evaluate whether the observed Cas10 dynamics occur within a single domain or across the whole subunit, we attached an acceptor fluorophore (Cy5) to two alternative positions in Cas10: L201 in its HD domain and L573 in its PALM domain (Figures S1B and S1C). Both labeled complexes displayed rapid and large-scale fluctuations in the FRET trajectories and broad FRET distributions (*E* spanning from 0.1 to 0.9; Figures 2G–2J, S3B, and S3C). Together, these results demonstrate that the entire Cas10 protein undergoes conformational fluctuations when bound to non-self RNA targets.

Distinct Behaviors of Cas10 on Self versus Non-self RNA
Next, we performed the same set of FRET measurements on the anti-tag RNA, which mimics transcripts derived from the host's own CRISPR loci. The FRET distribution for Csm5-labeled complexes on 5′-end-labeled anti-tag RNA exhibited a single peak at ∼0.25 (95% of the trajectories are static; Figures 3A and 3B), indistinguishable from that for the WT RNA (Figure 2B). The FRET distribution for Csm4-labeled complexes on 3′-end-labeled anti-tag RNA again showed a single peak (90% of the trajectories are static; Figures 3C and 3D), but with a modest increase in the FRET value of the peak center (*E* ∼0.28) compared to the corresponding distribution for the WT RNA (Figure 2D).
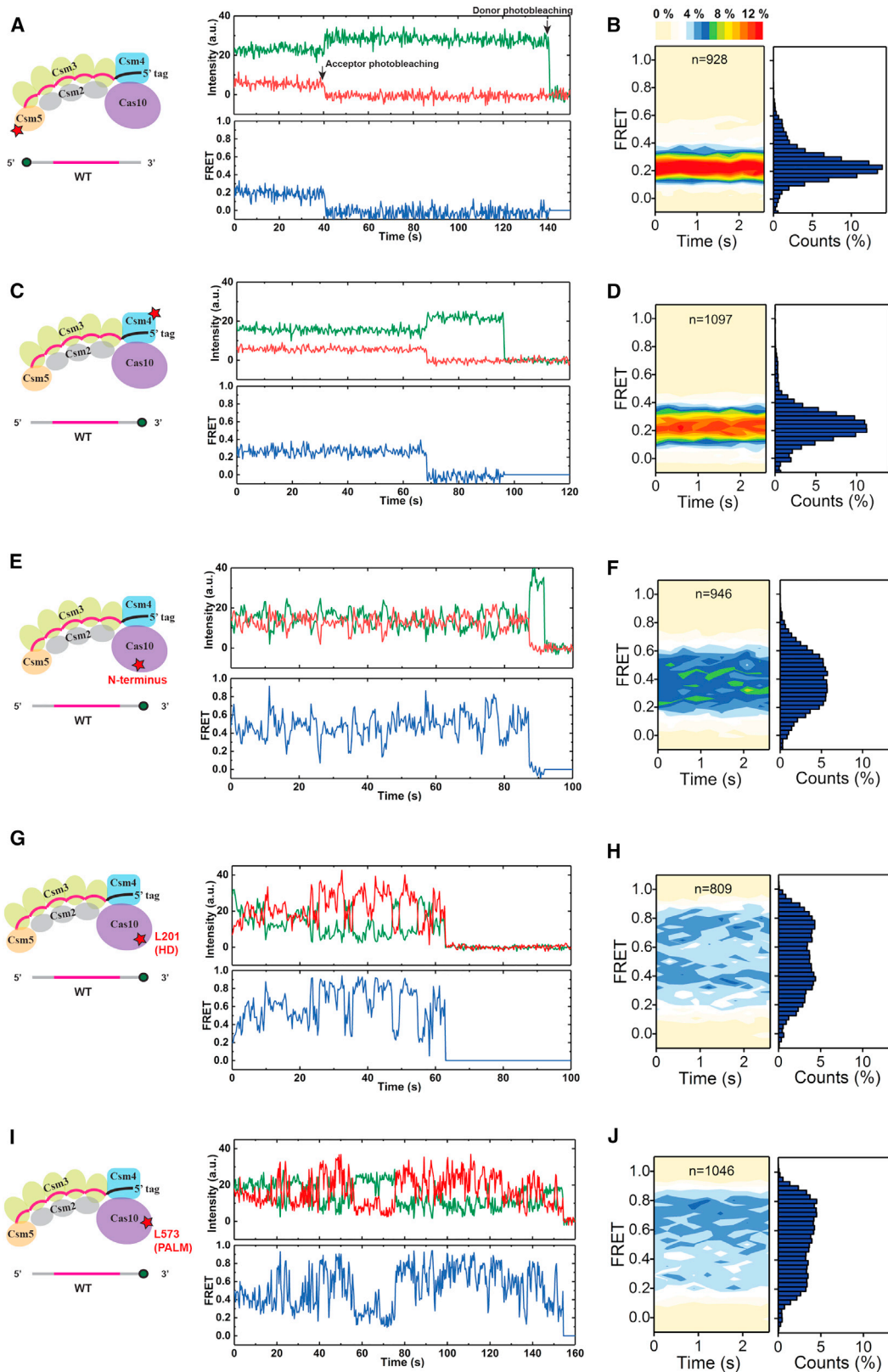
This difference can be rationalized by the base pairing between the crRNA tag and the 3′-flanking region of the anti-tag RNA, which conceivably brings the 3′ end of the RNA closer to Csm4 (Tamulaitis et al., 2017).

Strikingly, interrogation of Cas10-labeled complexes on the anti-tag RNA revealed a major difference. The vast majority (85%) of binding events of N-terminal-labeled Cas10 on 3′-end-labeled anti-tag RNA exhibited a stable, low-FRET state ($E \sim 0.29$) (Figures 3E and 3F), in stark contrast to the wide fluctuations observed in the corresponding FRET traces for the WT RNA (Figures 2E and 2F). Similarly, Cas10 with the acceptor fluorophore placed inside either its HD domain or its PALM domain showed a largely static behavior on the anti-tag RNA (Figure S4). Thus, complementarity between the crRNA tag and the 3′-flanking sequence of the anti-tag RNA constrains Cas10 in a stable, presumably inactive configuration.

We then sought to further dissect the sequence determinants in the 3′-flanking region of the target RNA that suppress the conformational fluctuations of Cas10. A structural model for a type III-A Cas10-Csm complex proposed that only four nucleotides (positions 4–7) of the 8-nt crRNA tag are available for base pairing with the target RNA (Kazlauskiene et al., 2016). We thus examined Cas10 dynamics on an RNA substrate with its 3′-flanking sequence complementary to the crRNA tag only at positions 4–7 (termed anti-tag$^{4-7}$; Figure 3G). Using N-terminus-labeled Cas10 and 3′-end-labeled Anti-tag$^{4-7}$ RNA, we obtained a FRET distribution that resembles the one for the fully complementary anti-tag RNA, displaying a dominant low-FRET peak (Figures 3F and 3H). We did observe a modest shoulder within higher FRET regions (Figure 3H), suggesting a slightly higher tendency of Cas10 to visit other states.

Self RNA Inhibits Activation of the Cas10-Csm Complex

To correlate the single-molecule data to *in vivo* immune responses elicited by the WT and anti-tag RNAs, we conducted a bacterial transformation assay to measure the strength of CRISPR immunity (Marraffini and Sontheimer, 2010; Samai et al., 2015) using the same target sequences as in the single-molecule experiments. In this assay, *Staphylococcus aureus* strains were transformed with two plasmids: (1) pCRISPR carrying an *S. epidermidis* type III-A CRISPR-Cas system with the *gp43* spacer or a control plasmid (pCRISPRΔspc) with a non-matching spacer and (2) a plasmid encoding either the WT

RNA (pTarget^{WT}) or the Anti-tag RNA (pTarget$^{Anti-tag}$) under the control of an anhydrotetracycline (aTc)-inducible promoter (Figure 4A). Activation of Cas10 by target RNA binding would lead to degradation of the target plasmid and inhibition of transformation.

In the absence of aTc, there was no target transcription to activate Cas10 and, therefore, no degradation of pTarget DNA. As expected, we measured a high efficiency of transformation for both pTarget^{WT} and pTarget$^{Anti-tag}$ (Figure 4B). In the presence of aTc, transformation of pTarget^{WT} was essentially abrogated (Figures 4B and 4C), suggesting effective elimination of the plasmid DNA by Cas10. In contrast, induction of pTarget$^{Anti-tag}$ transcription still resulted in a substantial number of transformants comparable to the pCRISPRΔspc control (Figures 4B and 4C), indicating that the CRISPR immunity is greatly diminished by the anti-tag RNA.

The *in vitro* and *in vivo* results together suggest that the distinct behavior of Cas10 on WT versus anti-tag RNA is correlated to the ability of the type III CRISPR-Cas system to provide immunity to the host cell; the stable FRET state observed with the anti-tag RNA likely represents an inactive configuration of Cas10, whereas WT RNA engagement unlocks Cas10 and prompts it to quickly access many conformational states, a subset of which enables the effector complex to degrade the invader plasmid.

Protospacer Mutations Differentially Modulate Cas10 Dynamics

We have shown that complementarity between the 3′-flanking region of the protospacer and the crRNA 5′ tag dramatically influences the behavior of Cas10. Next we investigated the effect of mismatches within the protospacer on Cas10 dynamics. We mutagenized the first (closest to the crRNA tag), second, or last 10-nt segments of the 35-nt protospacer sequence in order to create mismatches against the corresponding segment of the crRNA spacer. The mismatched RNA targets are termed MM1-10, MM11-20, and MM26-35, respectively (Figure 5A). Bulk biochemical experiments showed that mismatches specifically inhibit RNA cleavage within the mutated segment (Figure S5), confirming the requirement of base pairing between spacer and protospacer for RNA cleavage and the independent activities of the multiple copies of Csm3 (Staals et al., 2014).

We then performed single-molecule FRET assays to interrogate the interactions of the Cas10-Csm complex with the

Figure 2. Interaction between the Cas10-Csm Complex and Non-self RNA
(A) A representative time trajectory of donor (Cy3, green) and acceptor (AlexaFluor647, red) fluorescence intensities and the corresponding FRET values (blue) using AlexaFluor647-labeled Csm5 subunit and WT RNA labeled with Cy3 at its 5′ end.
(B) Contour plot and histogram for the FRET distribution from single-molecule trajectories described in (A) (n = 928; *n* denotes the number of molecules analyzed).
(C and D) A representative fluorescence and FRET trajectory (C) and the corresponding FRET contour plot and histogram (D) using AlexaFluor647-labeled Csm4 subunit and WT RNA labeled with Cy3 at its 3′ end (n = 1097).
(E and F) A representative fluorescence and FRET trajectory (E) and the corresponding FRET contour plot and histogram (F) using the Cas10 subunit labeled with AlexaFluor647 at its N terminus and WT RNA labeled with Cy3 at its 3′ end (n = 946).
(G and H) A representative fluorescence and FRET trajectory (G) and the corresponding FRET contour plot and histogram (H) using Cas10 labeled with Cy5 in the HD domain (position L201; n = 809).
(I and J) A representative fluorescence and FRET trajectory (I) and the corresponding FRET contour plot and histogram (J) using Cas10 labeled with Cy5 in the PALM domain (position L573; n = 1046).
The fluorescence lifetime was dependent on the laser power. Thus, the loss of fluorescence signal in the trajectories was likely due to dye photobleaching rather than complex dissociation.
See also Figures S1 and S3.
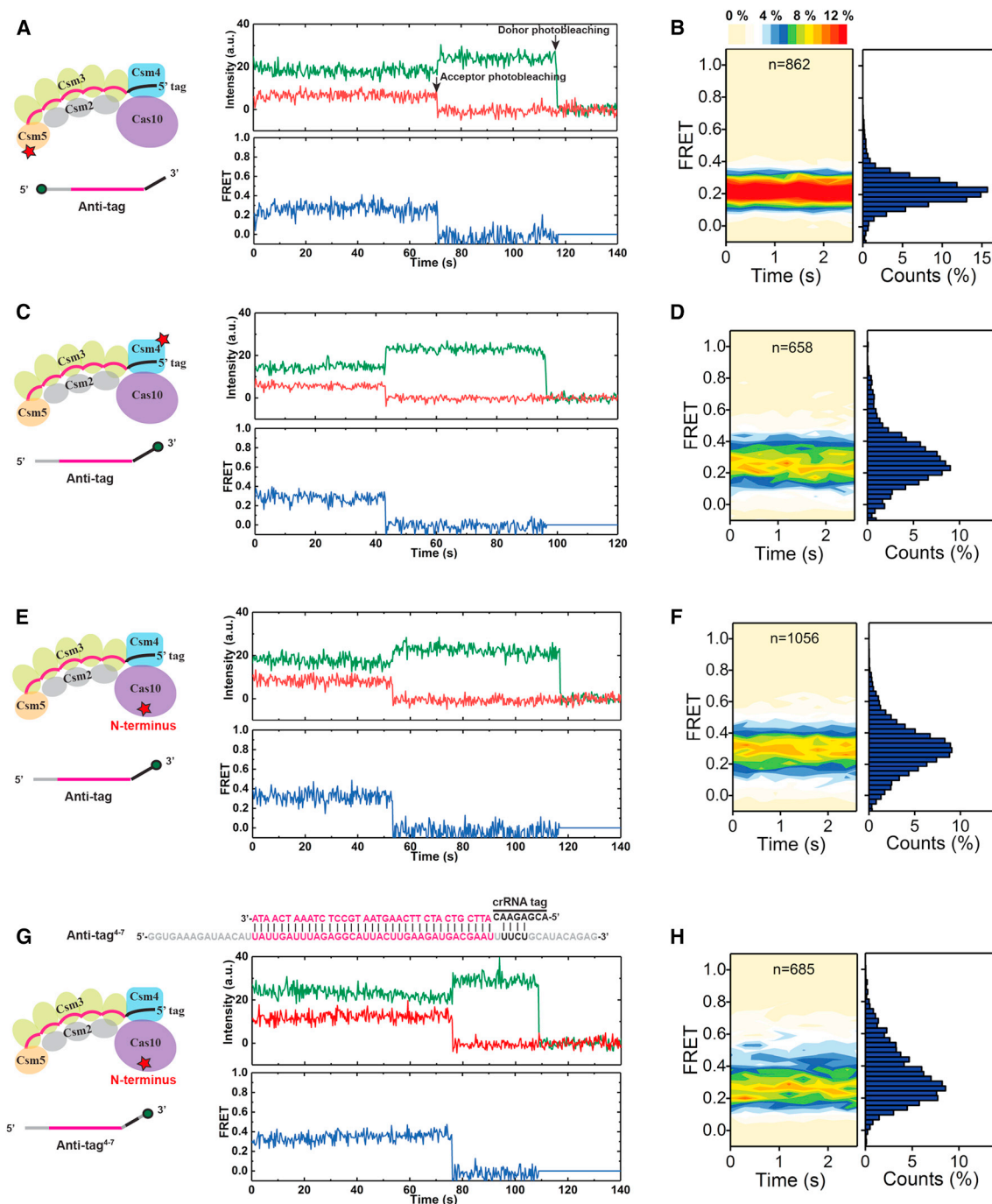
Figure 3. Interaction between the Cas10-Csm Complex and Self RNA

(A) A representative time trajectory of fluorescence intensities and FRET values using acceptor-labeled Csm5 subunit and anti-tag RNA labeled with FRET donor at its 5′ end.

(B) Contour plot and histogram for the FRET distribution from single-molecule trajectories described in (A) (n = 862).

(C and D) A representative fluorescence and FRET trajectory (C) and the corresponding FRET contour plot and histogram (D) using acceptor-labeled Csm4 subunit and anti-tag RNA labeled with donor at its 3′ end (n = 658).

(E and F) A representative fluorescence and FRET trajectory (E) and the corresponding FRET contour plot and histogram (F) using Cas10 labeled with acceptor at its N terminus (n = 1056).

(G and H) A representative fluorescence and FRET trajectory (G) and the corresponding FRET contour plot and histogram (H) using Cas10 labeled with acceptor at its N terminus and anti-tag[4−7] RNA labeled with donor at its 3′ end (n = 685).

See also Figures S1 and S4.
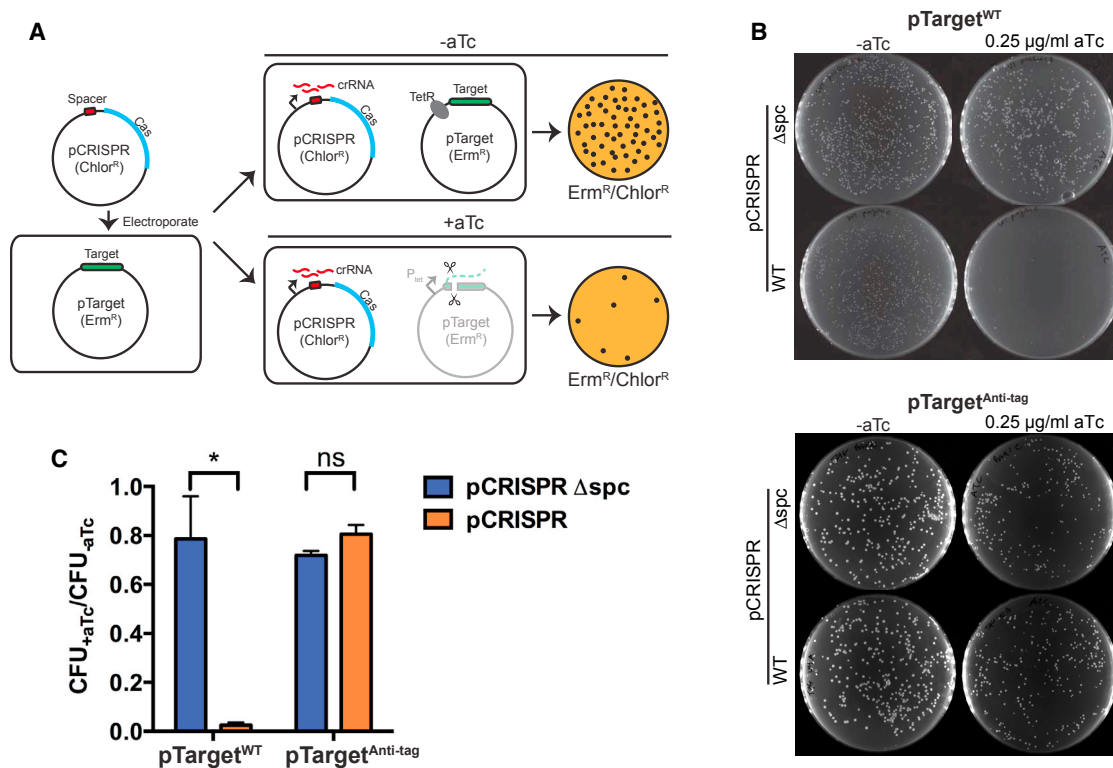
Figure 4. Evaluation of Type III CRISPR Immunity against Self versus Non-self Elements

(A) Schematic of the bacterial transformation assay. *S. aureus* strains with pTarget (Erm^R) were transformed with pCRISPR (Chlor^R) and plated onto chloramphenicol and erythromycin for double selection. In the absence of aTc, the tetracycline repressor (TetR) prevents target transcription. As a result, no CRISPR immunity is conferred against pTarget. In the presence of aTc, the target sequence on pTarget is transcribed, which triggers CRISPR immunity against the plasmid. Degradation of pTarget results in the loss of erythromycin resistance, thereby reducing the transformation efficiency.

(B) Representative plates of staphylococci colonies under different targeting conditions. In the presence of aTc, transformation of pTarget^{WT} plasmid was greatly diminished, indicating effective immunity induced by WT RNA transcription. By contrast, pTarget$^{Anti-tag}$ plasmid remained at a similar high level of transformation as the non-induction condition, suggesting impaired CRISPR immunity caused by the anti-tag RNA. As a control, both plasmids had similar high efficiencies of transformation into cells harboring pCRISPRΔspc.

(C) Transformation efficiencies of pTarget^{WT} and pTarget$^{Anti-tag}$ into cells containing the pCRISPR (orange bars) or pCRISPRΔspc (blue bars) plasmid. The transformation efficiency is calculated as the ratio of colony-forming units (CFU) per microgram of plasmid DNA transformed in the presence and absence of aTc. Data are represented as mean ± SEM (three independent experiments).

mismatched RNA targets. We used complexes harboring RNase-deficient Csm3^{D32A} mutants in order to monitor the behavior of Cas10 in a Mg^{2+}-containing buffer (Figure S2B). Cas10 exhibited conformational fluctuations on all mismatched targets (73% of the trajectories are dynamic for MM1-10; 78% for MM11-20; 76% for MM26-35; Figures 5B and S6A), similar to the WT RNA but in opposition to the anti-tag RNA. Notably, the FRET distribution varied among different targets, shifting toward lower FRET values and deviating further from the distribution for the WT RNA as the mismatches move from tag-distal to tag-proximal regions (Figure 5C).

To quantify the effects of mismatches on Cas10 dynamics, we employed hidden-Markov-modeling (HMM) analysis (McKinney et al., 2006) to identify distinct FRET states in the single-molecule trajectories and transitions between them (orange lines in Figures 5B and S6A). The resulting transition density plots (TDP) display the relative frequencies of transitions binned by the FRET values before and after each transition. We separated

the HMM-fitted states into four groups: G_1 ($E \leq 0.3$), G_2 ($0.3 < E \leq 0.4$), G_3 ($0.4 < E \leq 0.55$), and G_4 ($E > 0.55$) (Figure 5D). A comparison of TDP for different targets revealed that the WT, MM26-35, MM11-20, and MM1-10 RNA exhibit transition frequencies between the high FRET groups G_3 and G_4 (f_{3-4} and f_{4-3}) in a descending order (Figures 5E and S6B). The opposite pattern was observed for the transition frequencies between the low FRET groups G_1 and G_2 (f_{1-2} and f_{2-1}) (Figure 5E). These results demonstrate that protospacer mutations differentially influence the conformational distribution of Cas10, with tag-proximal mutations (MM1-10) having the strongest effect and tag-distal ones (MM26-35) the weakest.

Conformational Distribution of Cas10 Correlates with CRISPR Interference Activity

To investigate the relationship between the conformational distribution of Cas10 and the strength of type III CRISPR immunity, we next performed the transformation assay described in
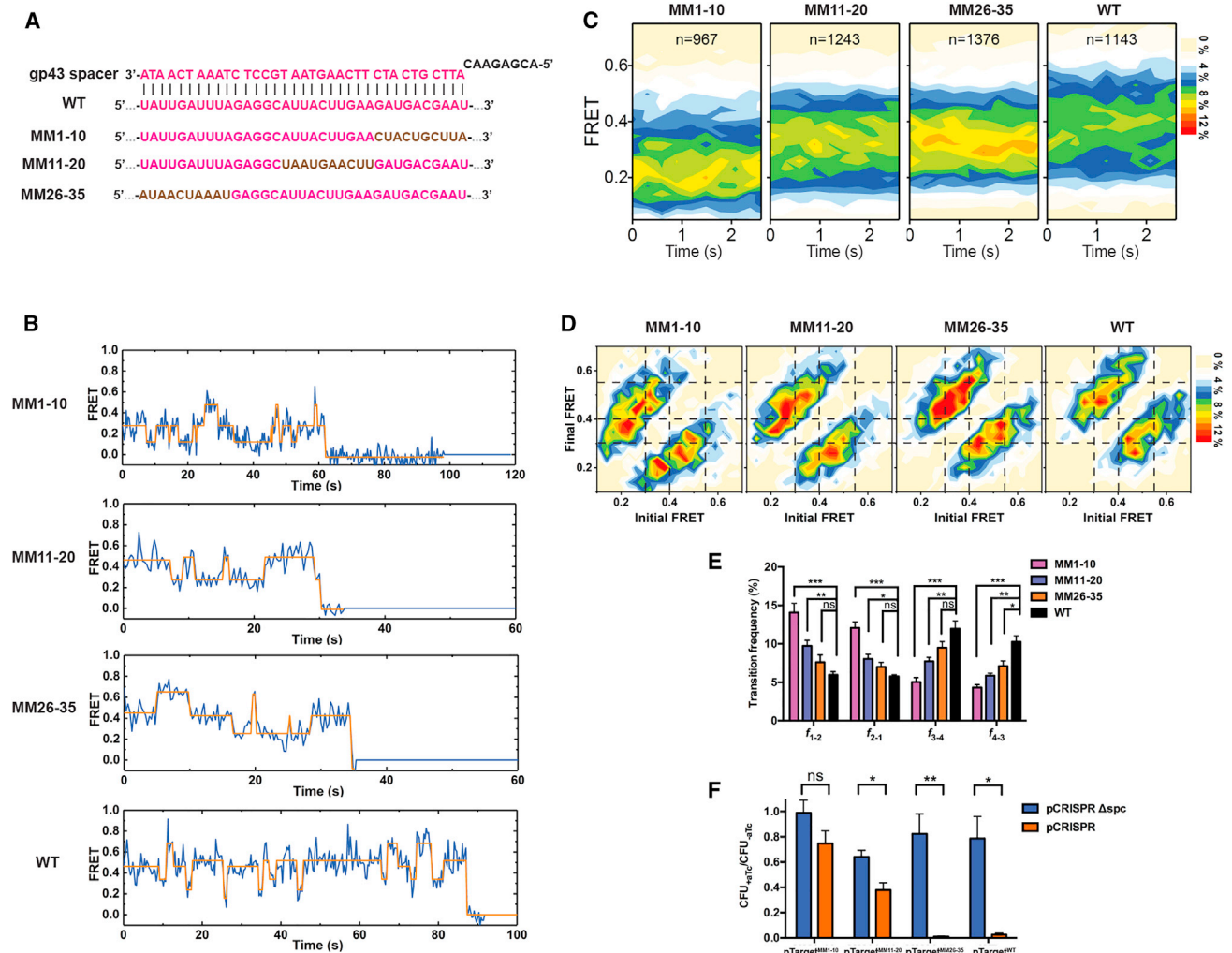
Figure 5. Protospacer Mutations Modulate Cas10 Dynamics and Type III CRISPR Immunity

(A) Sequences of different mismatched RNA targets. Mutated regions are shown in brown.

(B) Example FRET trajectories showing Cas10 dynamics on WT and mismatched RNA targets. FRET donor and acceptor were placed at the 3′ end of RNA and the N terminus of Cas10, respectively. Orange lines represent idealized FRET states from hidden-Markov-modeling (HMM) analysis.

(C) FRET contour plots for WT and mismatched RNA targets.

(D) Transition density plots for WT and mismatched RNA targets. Dashed lines separate distinct FRET groups: G_1 ($E \leq 0.3$), G_2 ($0.3 < E \leq 0.4$), G_3 ($0.4 < E \leq 0.55$), and G_4 ($E > 0.55$).

(E) Transition frequencies between FRET groups for different RNA targets. For example, f_{1-2} denotes the transition frequency from G_1 to G_2.

(F) Transformation efficiencies of pTarget^{WT}, pTarget^{MM1-10}, pTarget$^{MM11-20}$, and pTarget$^{MM26-35}$ into cells containing the pCRISPR plasmid (orange bars). A smaller value corresponds to a stronger immune response. The same measurements were repeated with pCRISPRΔspc-containing cells as negative controls (blue bars).

Data are represented as mean ± SEM.

See also Figures S5 and S6.

Figure 4A with pTarget plasmids encoding the mismatched RNA targets (pTarget^{MM1-10}, pTarget$^{MM11-20}$, and pTarget$^{MM26-35}$). The strength of immunity—reflected by the pTarget transformation efficiency—decreases as the target mismatches move from tag-distal (MM26-35) to tag-proximal (MM1-10) regions (Figure 5F, orange bars). Importantly, this trend matches well with the gradual shift in the distribution of Cas10's conformational states obtained from single-molecule FRET measurements (Figures 5C–5E). Hence, the conformational distribution of Cas10 is

correlated with *in vivo* CRISPR interference activity: the more time Cas10 spends in the high FRET states, the stronger immunity the Cas10-Csm complex confers.

Single-Stranded DNA and ATP Enriches Specific Cas10 Conformations

Among the various RNA targets studied here, anti-tag and MM1-10 elicited the weakest immune responses (Figures 4C and 5F). They also resulted in predominantly low FRET
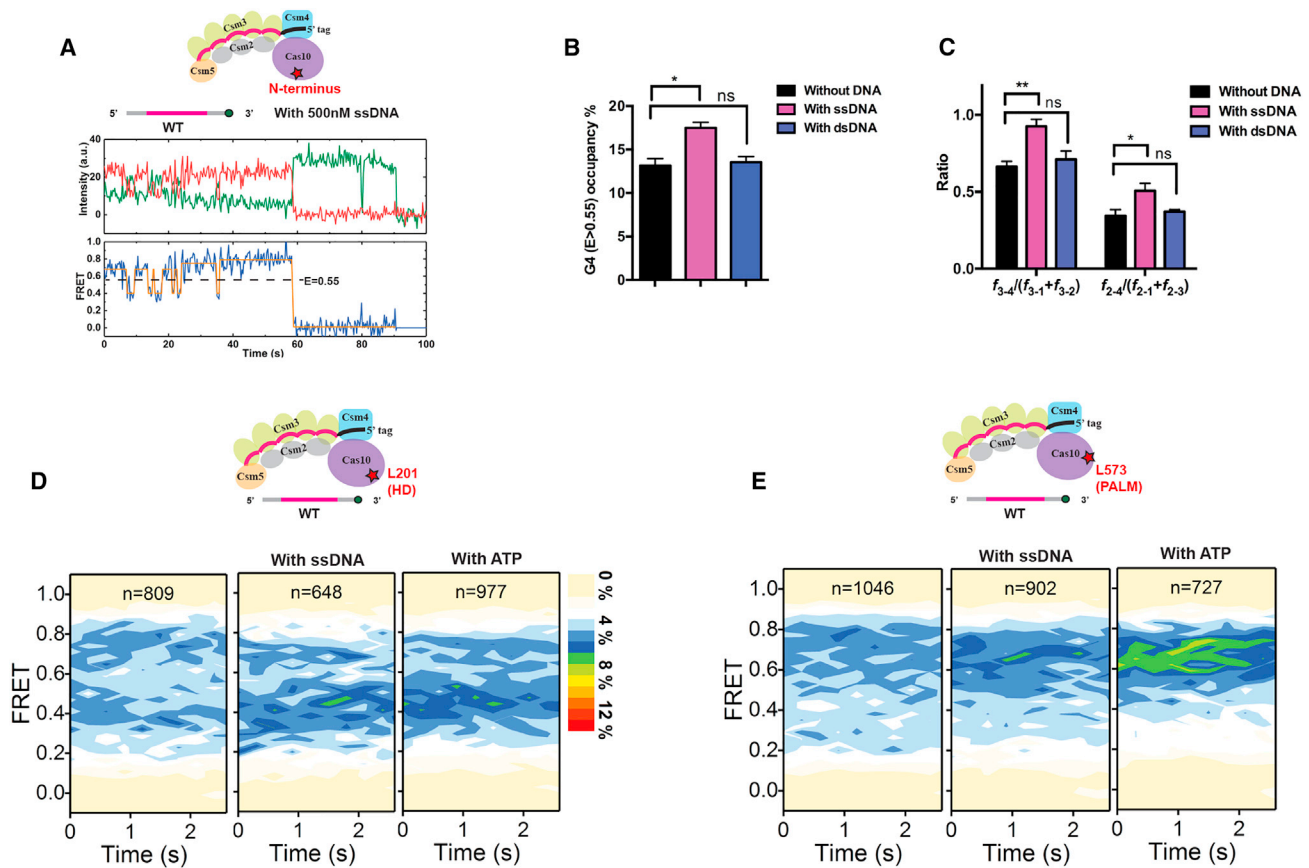
Figure 6. Effects of DNA and ATP on Cas10's Conformational Distribution

(A) A representative fluorescence and FRET trajectory using Cas10 labeled with acceptor at its N terminus and WT RNA labeled with donor at its 3′ end in the presence of 500 nM ssDNA.

(B) The fraction of time the complex spent within the highest FRET group G_4 ($E > 0.55$) in the absence of DNA (black), in the presence of 500 nM ssDNA (magenta), and in the presence of 500 nM dsDNA (blue).

(C) The likelihood of complexes in G_2 or G_3 transitioning to G_4—shown as the ratio of transition frequencies to G_4 and to the other groups—with or without DNA.

(D) FRET contour plots using Cas10 labeled with FRET acceptor in its HD domain and donor-labeled WT RNA (left), in the presence of 500 nM ssDNA (middle), and in the presence of 2.5 mM ATP (right).

(E) Same as above, except using Cas10 labeled with acceptor in its PALM domain.

Data are represented as mean ± SEM.

See also Figure S7.

populations ($E < 0.4$) upon Cas10-Csm binding (Figures 3F and 5C). On the contrary, WT and MM26-35 RNAs induced Cas10 to occupy higher FRET states and, accordingly, triggered robust anti-plasmid immunity (Figures 5C–5F). These results prompted us to propose that Cas10 becomes DNase-active when accessing the higher FRET states. To further determine the identity of the active state of Cas10, we reasoned that it would be enriched by the engagement of DNA substrates. Thus, we examined the effect of DNA on the conformational distribution of Cas10.

Using the Cas10-N terminus/RNA-3′ end labeling scheme, we obtained single-molecule FRET trajectories with the WT RNA target in the presence of 55-nt-long linear ssDNA that contains the same base sequence as the WT RNA (Figures 6A and S7A). The trajectories remained highly dynamic, but the relative population of the highest FRET group G_4 ($E > 0.55$) significantly increased

(Figure 6B). Moreover, TDP analysis revealed that ssDNA caused a higher probability for effector complexes residing in other FRET groups to transition to G_4 (Figures 6C and S7B). Interestingly, double-stranded DNA (dsDNA) of the same length and sequence had little effect on the FRET distribution (Figures 6B and 6C), corroborating previous reports that dsDNA is not a good substrate for Cas10 (Estrella et al., 2016; Kazlauskiene et al., 2016). These results strongly suggest that G_4 represents the DNase-active form of the Cas10-Csm effector complex.

We then assessed the impact of ssDNA on Cas10 dynamics using the other two labeling positions, L201 in the HD domain and L573 in the PALM domain. We found that ssDNA modestly enriches specific FRET states ($E \sim 0.42$ for L201; $E \sim 0.67$ for L573; Figures 6D and 6E). Given that Cas10 harbors another activity— converting ATP to cOA—we also examined the effect of ATP; we found that ATP causes a similar, if not stronger, level
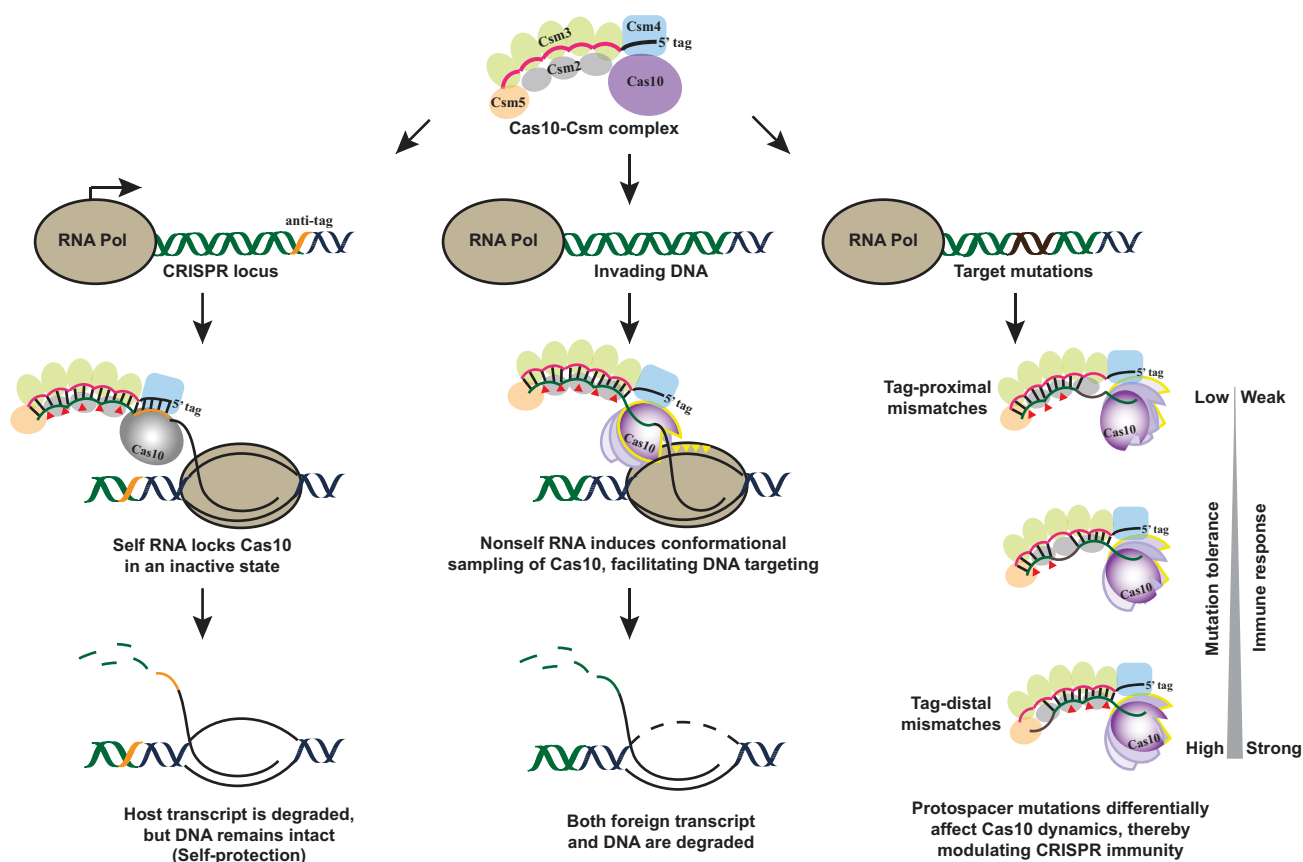
Figure 7. Model for Self versus Non-self Discrimination and Target Mutation Tolerance in Type III CRISPR-Cas Immunity

Complementarity between the crRNA 5′ tag and the anti-tag sequence within the RNA transcribed from the host's CRISPR locus locks Cas10 in an inactive state and suppresses CRISPR immunity. On the contrary, transcripts derived from foreign elements lack sequence homology to the crRNA tag, thereby enabling conformational fluctuations of Cas10 and conferring robust immunity. Mutations in the protospacer sequence of the target differentially modulate the behavior of Cas10: tag-proximal mismatches depopulate Cas10 from its active state, whereas tag-distal ones yield WT-like dynamics. As a result, type III CRISPR-Cas systems exhibit broad target specificity and can tolerate target mutations to varying degrees.

of consolidation in the FRET distribution, especially in the PALM-domain-labeled complex (Figure 6E), consistent with previous studies that mapped the ATP conversion activity to the PALM domain of Cas10 (Kazlauskiene et al., 2017; Niewoehner et al., 2017).

DISCUSSION

Type III CRISPR-Cas systems employ an elaborate targeting mechanism to degrade both the invading DNA and its RNA transcripts. The extraordinary complexity compared to other CRISPR systems allows for exquisite spatiotemporal control of the immune response (Tamulaitis et al., 2017). Here we present, to our knowledge, the first single-molecule study of type III CRISPR immunity, which provides a molecular basis for the discrimination between self and non-self genetic elements and the unusually high tolerance to target mutations by type III systems (Figure 7). Central to our findings is the remarkable conformational flexibility of Cas10, the signature subunit of type III effector complexes. Our results suggest that the confor-

mational distribution of Cas10 plays a major role in regulating the CRISPR interference activity of the effector complex.

Discrimination Between Self and Non-self

Unlike type I (Cascade), II (Cas9), and V (Cpf1) systems, which recognize specific PAM sequences to license foreign DNA, type III systems recognize specific protospacer flanking sequences—ones that are complementary to the crRNA tag—to identify self RNA (Mohanraju et al., 2016). The molecular underpinning of this unique discrimination mechanism has remained puzzling, because the type III machinery displays non-discriminatory binding and cleavage activities on any RNA that contains the protospacer sequence—self or non-self. Here we show that the discriminatory step is manifested in the distinctive Cas10 conformational dynamics. Foreign RNA binding enables Cas10 to quickly sample a large conformational space, including a plausible DNase-active configuration. Engagement with DNA substrates further enhances Cas10's propensity for residing at the active configuration. On the other hand, self (anti-tag) RNA dramatically represses the structural fluctuations of Cas10 and

stabilizes it in an inactive configuration. As a result, the occupancy of Cas10 at the active state is greatly diminished, thereby effectively preventing self-targeting. A comparison between anti-tag and anti-tag[4-7] RNA results indicates that base pairing at nucleotide positions 4–7 of the crRNA tag is the main determinant for suppressing Cas10's conformational flexibility; but other positions in the 3′-flanking region of the target RNA may also play a minor role in self versus non-self discrimination. High-resolution structures are needed to provide atomic details of the self-RNA-bound Cas10-Csm complex and explain how base pairing between the crRNA tag and the target RNA 3′-flanking sequence deactivates Cas10.

Mutation Tolerance

Phages are constantly evolving to avoid elimination by prokaryotic defense systems. Type I and II CRISPR-Cas systems are extremely sensitive to mutations in the PAM-proximal region of the protospacer, also known as the seed region (Semenova et al., 2011; Wiedenheft et al., 2011). Single-nucleotide mutations in the seed or PAM region abolish immunity and cause viral escape. Mismatches in PAM-distal regions are tolerated to some extent, but they still cause compromised immune responses (Wu et al., 2014). Such strict sequence requirements are related to the process of target recognition, in which initial PAM binding leads to directional unwinding of the dsDNA and formation of the RNA:DNA heteroduplex (R-loop) from the seed throughout the protospacer. Target mutations inhibit R-loop formation and reduce its stability, thereby compromising the efficiency of CRISPR interference (Blosser et al., 2015; Szczelkun et al., 2014). In comparison, the entire single-stranded RNA target sequence in type III systems is directly available for base pairing with crRNA, circumventing the need for duplex unwinding. Hence any single-point mutation is unlikely to significantly affect the affinity between the target RNA and the effector complex.

Nonetheless, mismatches do affect type III interference efficiency to varying degrees (Pyenson et al., 2017). Our data offer an explanation for this effect: mismatches in different regions of the protospacer differentially alter the conformational distribution of Cas10. For the *gp43* spacer used in this work, mismatches from tag-distal to tag-proximal regions increasingly populate Cas10 in the inactive mode, resulting in decreasing immunity observed *in vivo*. Based on the few spacers examined in our current and prior studies (Pyenson et al., 2017), this spatial pattern of mismatch sensitivity seems to be generalizable. The quantitative level of inhibition by mismatches, on the other hand, is likely spacer specific.

The base-pairing status of the spacer:protospacer region, which resides within the backbone of the effector complex, allosterically modulates the behavior of Cas10. But none of the mismatched targets abolishes the catalytically active population of Cas10 to the same extent as the anti-tag RNA. Consequently, type III systems display broad tolerance to target mutations. Viral escape necessitates a full deletion of the target (Pyenson et al., 2017) or a particular set of mutations that create a perfect match with the crRNA tag, both of which are rare events. Therefore, type III CRISPR-Cas systems have evolved an elegant strategy that provides robust immune responses and greatly limits viral escape while at the same time effectively avoiding autoimmunity.

Internal Dynamics of the Effector Complex Dictate CRISPR-Cas Immunity

The striking correlation between the conformational distribution of Cas10 and the strength of type III CRISPR immunity enabled us to deduce the active and inactive states of the Cas10-Csm complex. The two types of substrates of Cas10's enzymatic reactions—ssDNA and ATP—both influence Cas10's highly dynamic conformational fluctuations, which take place across the whole subunit. Such influence would be difficult to characterize quantitatively by methods other than real-time single-molecule measurements. Future experiments of this kind will elucidate the specific and distinct conformational states associated with DNA cleavage and ATP conversion activities. Notably, the dynamic nature of the effector complex appears to be modular; the other non-catalytic scaffold subunits, such as Csm4 and Csm5, are largely immobile with respect to the RNA target.

The correlation between internal dynamics and enzymatic activity has also been reported for the type II single-subunit effector Cas9 (Dagdas et al., 2017; Sternberg et al., 2015; Yang et al., 2018). The DNA cleavage activity of Cas9 scales with the fraction of time it spends in the DNase-active state. Target mismatches prevent transition from a checkpoint state to the active state. Similarly, the Cse1 subunit of the type I Cascade complex—the putative homolog of Cas10 (Makarova et al., 2011)—is also conformationally flexible (Krivoy et al., 2018; Xue et al., 2016). This flexibility is exploited in the Cas3 recruitment process to reduce off targeting (Xiao et al., 2018). Together, these parallels imply that the employment of conformational flexibility to control function is a common feature for diverse CRISPR-Cas systems.

In summary, we showed that the conformational fluctuation of Cas10 is exquisitely regulated by the complementarity between the target RNA and crRNA. As such, Cas10's activity is controlled as a gradual dimmer rather than an on-off switch, allowing the host to tune its immune response to an optimal level according to the particular circumstance. The single-molecule imaging platform established here can be used to study Cas10-Csm/Cmr complexes from other species. It will also be interesting to directly observe the concerted action of the transcription complex and the type III CRISPR machinery.

STAR★METHODS

Detailed methods are provided in the online version of this paper and include the following:

- KEY RESOURCES TABLE
- CONTACT FOR REAGENT AND RESOURCE SHARING
- EXPERIMENTAL MODEL AND SUBJECT DETAILS
  - Bacterial strains and growth conditions
- METHOD DETAILS
  - Plasmid construction
  - Protein expression and purification
  - Site-specific fluorescent labeling
  - Bulk RNA cleavage assay
  - Bacterial transformation assay
  - Single-molecule experiments
- QUANTIFICATION AND STATISTICAL ANALYSIS
- DATA AND SOFTWARE AVAILABILITY

REFERENCES

Barrangou, R., Fremaux, C., Deveau, H., Richards, M., Boyaval, P., Moineau, S., Romero, D.A., and Horvath, P. (2007). CRISPR provides acquired resistance against viruses in prokaryotes. Science 315, 1709–1712.

Blosser, T.R., Loeff, L., Westra, E.R., Vlot, M., Künne, T., Sobota, M., Dekker, C., Brouns, S.J.J., and Joo, C. (2015). Two distinct DNA binding modes guide dual roles of a CRISPR-Cas protein complex. Mol. Cell 58, 60–70.

Boehm, T. (2006). Quality control in self/nonself discrimination. Cell 125, 845–858.

Chen, J.S., Dagdas, Y.S., Kleinstiver, B.P., Welch, M.M., Sousa, A.A., Harrington, L.B., Sternberg, S.H., Joung, J.K., Yildiz, A., and Doudna, J.A. (2017). Enhanced proofreading governs CRISPR-Cas9 targeting accuracy. Nature 550, 407–410.

Dagdas, Y.S., Chen, J.S., Sternberg, S.H., Doudna, J.A., and Yildiz, A. (2017). A conformational checkpoint between DNA binding and cleavage by CRISPR-Cas9. Sci. Adv. 3, eaao0027.

Deng, L., Garrett, R.A., Shah, S.A., Peng, X., and She, Q. (2013). A novel interference mechanism by a type IIIB CRISPR-Cmr module in Sulfolobus. Mol. Microbiol. 87, 1088–1099.

Dillard, K.E., Brown, M.W., Johnson, N.V., Xiao, Y., Dolan, A., Hernandez, E., Dahlhauser, S.D., Kim, Y., Myler, L.R., Anslyn, E.V., et al. (2018). Assembly and Translocation of a CRISPR-Cas Primed Acquisition Complex. Cell 175, 934–946.e15.

Elmore, J.R., Sheppard, N.F., Ramia, N., Deighan, T., Li, H., Terns, R.M., and Terns, M.P. (2016). Bipartite recognition of target RNAs activates DNA cleavage by the Type III-B CRISPR-Cas system. Genes Dev. 30, 447–459.

Estrella, M.A., Kuo, F.T., and Bailey, S. (2016). RNA-activated DNA cleavage by the Type III-B CRISPR-Cas effector complex. Genes Dev. 30, 460–470.

Gasiunas, G., Barrangou, R., Horvath, P., and Siksnys, V. (2012). Cas9-crRNA ribonucleoprotein complex mediates specific DNA cleavage for adaptive immunity in bacteria. Proc. Natl. Acad. Sci. USA 109, E2579–E2586.

Goldberg, G.W., Jiang, W., Bikard, D., and Marraffini, L.A. (2014). Conditional tolerance of temperate phages via transcription-dependent CRISPR-Cas targeting. Nature 514, 633–637.

Hale, C.R., Zhao, P., Olson, S., Duff, M.O., Graveley, B.R., Wells, L., Terns, R.M., and Terns, M.P. (2009). RNA-guided RNA cleavage by a CRISPR RNA-Cas protein complex. Cell 139, 945–956.

Hatoum-Aslan, A., Samai, P., Maniv, I., Jiang, W., and Marraffini, L.A. (2013). A ruler protein in a complex for antiviral defense determines the length of small interfering CRISPR RNAs. J. Biol. Chem. 288, 27888–27897.

Horinouchi, S., and Weisblum, B. (1982). Nucleotide sequence and functional map of pE194, a plasmid that specifies inducible resistance to macrolide, lincosamide, and streptogramin type B antibodies. J. Bacteriol. 150, 804–814.

Jeon, Y., Choi, Y.H., Jang, Y., Yu, J., Goo, J., Lee, G., Jeong, Y.K., Lee, S.H., Kim, I.S., Kim, J.S., et al. (2018). Direct observation of DNA target searching and cleavage by CRISPR-Cas12a. Nat. Commun. 9, 2777.

Jiang, W., Samai, P., and Marraffini, L.A. (2016). Degradation of Phage Transcripts by CRISPR-Associated RNases Enables Type III CRISPR-Cas Immunity. Cell 164, 710–721.

Juette, M.F., Terry, D.S., Wasserman, M.R., Altman, R.B., Zhou, Z., Zhao, H., and Blanchard, S.C. (2016). Single-molecule imaging of non-equilibrium molecular ensembles on the millisecond timescale. Nat. Methods 13, 341–344.

Kazlauskiene, M., Tamulaitis, G., Kostiuk, G., Venclovas, Č., and Siksnys, V. (2016). Spatiotemporal Control of Type III-A CRISPR-Cas Immunity: Coupling DNA Degradation with the Target RNA Recognition. Mol. Cell 62, 295–306.

Kazlauskiene, M., Kostiuk, G., Venclovas, Č., Tamulaitis, G., and Siksnys, V. (2017). A cyclic oligonucleotide signaling pathway in type III CRISPR-Cas systems. Science 357, 605–609.

Koonin, E.V., Makarova, K.S., and Zhang, F. (2017). Diversity, classification and evolution of CRISPR-Cas systems. Curr. Opin. Microbiol. 37, 67–78.

Kreiswirth, B.N., Löfdahl, S., Betley, M.J., O'Reilly, M., Schlievert, P.M., Bergdoll, M.S., and Novick, R.P. (1983). The toxic shock syndrome exotoxin structural gene is not detectably transmitted by a prophage. Nature 305, 709–712.

Krivoy, A., Rutkauskas, M., Kuznedelov, K., Musharova, O., Rouillon, C., Severinov, K., and Seidel, R. (2018). Primed CRISPR adaptation in Escherichia coli cells does not depend on conformational changes in the Cascade effector complex detected in Vitro. Nucleic Acids Res. 46, 4087–4098.

Lim, Y., Bak, S.Y., Sung, K., Jeong, E., Lee, S.H., Kim, J.S., Bae, S., and Kim, S.K. (2016). Structural roles of guide RNAs in the nuclease activity of Cas9 endonuclease. Nat. Commun. 7, 13350.

Loeff, L., Brouns, S.J.J., and Joo, C. (2018). Repetitive DNA Reeling by the Cascade-Cas3 Complex in Nucleotide Unwinding Steps. Mol. Cell 70, 385–394.e3.

Makarova, K.S., Aravind, L., Wolf, Y.I., and Koonin, E.V. (2011). Unification of Cas protein families and a simple scenario for the origin and evolution of CRISPR-Cas systems. Biol. Direct 6, 38.

Manica, A., Zebec, Z., Steinkellner, J., and Schleper, C. (2013). Unexpectedly broad target recognition of the CRISPR-mediated virus defence system in the archaeon Sulfolobus solfataricus. Nucleic Acids Res. 41, 10509–10517.

Maniv, I., Jiang, W., Bikard, D., and Marraffini, L.A. (2016). Impact of Different Target Sequences on Type III CRISPR-Cas Immunity. J. Bacteriol. 198, 941–950.

Marraffini, L.A., and Sontheimer, E.J. (2008). CRISPR interference limits horizontal gene transfer in staphylococci by targeting DNA. Science 322, 1843–1845.

Marraffini, L.A., and Sontheimer, E.J. (2010). Self versus non-self discrimination during CRISPR RNA-directed immunity. Nature 463, 568–571.

McKinney, S.A., Joo, C., and Ha, T. (2006). Analysis of single-molecule FRET trajectories using hidden Markov modeling. Biophys. J. *91*, 1941–1951.

Mohanraju, P., Makarova, K.S., Zetsche, B., Zhang, F., Koonin, E.V., and van der Oost, J. (2016). Diverse evolutionary roots and mechanistic variations of the CRISPR-Cas systems. Science *353*, aad5147.

Mojica, F.J., Díez-Villaseñor, C., García-Martínez, J., and Almendros, C. (2009). Short motif sequences determine the targets of the prokaryotic CRISPR defence system. Microbiology *155*, 733–740.

Niewoehner, O., Garcia-Doval, C., Rostøl, J.T., Berk, C., Schwede, F., Bigler, L., Hall, J., Marraffini, L.A., and Jinek, M. (2017). Type III CRISPR-Cas systems produce cyclic oligoadenylate second messengers. Nature *548*, 543–548.

Osawa, T., Inanaga, H., Sato, C., and Numata, T. (2015). Crystal structure of the CRISPR-Cas RNA silencing Cmr complex bound to a target analog. Mol. Cell *58*, 418–430.

Osuka, S., Isomura, K., Kajimoto, S., Komori, T., Nishimasu, H., Shima, T., Nureki, O., and Uemura, S. (2018). Real-time observation of flexible domain movements in CRISPR-Cas9. EMBO J. *37*, e96941.

Peng, W., Feng, M., Feng, X., Liang, Y.X., and She, Q. (2015). An archaeal CRISPR type III-B system exhibiting distinctive RNA targeting features and mediating dual RNA and DNA interference. Nucleic Acids Res. *43*, 406–417.

Pyenson, N.C., and Marraffini, L.A. (2017). Type III CRISPR-Cas systems: when DNA cleavage just isn't enough. Curr. Opin. Microbiol. *37*, 150–154.

Pyenson, N.C., Gayvert, K., Varble, A., Elemento, O., and Marraffini, L.A. (2017). Broad Targeting Specificity during Bacterial Type III CRISPR-Cas Immunity Constrains Viral Escape. Cell Host Microbe *22*, 343–353.e3.

Redding, S., Sternberg, S.H., Marshall, M., Gibb, B., Bhat, P., Guegler, C.K., Wiedenheft, B., Doudna, J.A., and Greene, E.C. (2015). Surveillance and Processing of Foreign DNA by the Escherichia coli CRISPR-Cas System. Cell *163*, 854–865.

Rouillon, C., Athukoralage, J.S., Graham, S., Grüschow, S., and White, M.F. (2018). Control of cyclic oligoadenylate synthesis in a type III CRISPR system. eLife *7*, e36734.

Rutkauskas, M., Sinkunas, T., Songailiene, I., Tikhomirova, M.S., Siksnys, V., and Seidel, R. (2015). Directional R-Loop Formation by the CRISPR-Cas Surveillance Complex Cascade Provides Efficient Off-Target Site Rejection. Cell Rep. *10*, 1534–1543.

Samai, P., Pyenson, N., Jiang, W., Goldberg, G.W., Hatoum-Aslan, A., and Marraffini, L.A. (2015). Co-transcriptional DNA and RNA Cleavage during Type III CRISPR-Cas Immunity. Cell *161*, 1164–1174.

Semenova, E., Jore, M.M., Datsenko, K.A., Semenova, A., Westra, E.R., Wanner, B., van der Oost, J., Brouns, S.J., and Severinov, K. (2011). Interference by clustered regularly interspaced short palindromic repeat (CRISPR) RNA is governed by a seed sequence. Proc. Natl. Acad. Sci. USA *108*, 10098–10103.

Singh, D., Sternberg, S.H., Fei, J., Doudna, J.A., and Ha, T. (2016). Real-time observation of DNA recognition and rejection by the RNA-guided endonuclease Cas9. Nat. Commun. *7*, 12778.

Singh, D., Mallon, J., Poddar, A., Wang, Y., Tippana, R., Yang, O., Bailey, S., and Ha, T. (2018). Real-time observation of DNA target interrogation and product release by the RNA-guided endonuclease CRISPR Cpf1 (Cas12a). Proc. Natl. Acad. Sci. USA *115*, 5444–5449.

Staals, R.H.J., Agari, Y., Maki-Yonekura, S., Zhu, Y., Taylor, D.W., van Duijn, E., Barendregt, A., Vlot, M., Koehorst, J.J., Sakamoto, K., et al. (2013). Structure and activity of the RNA-targeting Type III-B CRISPR-Cas complex of Thermus thermophilus. Mol. Cell *52*, 135–145.

Staals, R.H., Zhu, Y., Taylor, D.W., Kornfeld, J.E., Sharma, K., Barendregt, A., Koehorst, J.J., Vlot, M., Neupane, N., Varossieau, K., et al. (2014). RNA targeting by the type III-A CRISPR-Cas Csm complex of Thermus thermophilus. Mol. Cell *56*, 518–530.

Sternberg, S.H., Redding, S., Jinek, M., Greene, E.C., and Doudna, J.A. (2014). DNA interrogation by the CRISPR RNA-guided endonuclease Cas9. Nature *507*, 62–67.

Sternberg, S.H., LaFrance, B., Kaplan, M., and Doudna, J.A. (2015). Conformational control of DNA target cleavage by CRISPR-Cas9. Nature *527*, 110–113.

Szczelkun, M.D., Tikhomirova, M.S., Sinkunas, T., Gasiunas, G., Karvelis, T., Pschera, P., Siksnys, V., and Seidel, R. (2014). Direct observation of R-loop formation by single RNA-guided Cas9 and Cascade effector complexes. Proc. Natl. Acad. Sci. USA *111*, 9798–9803.

Tamulaitis, G., Kazlauskiene, M., Manakova, E., Venclovas, Č., Nwokeoji, A.O., Dickman, M.J., Horvath, P., and Siksnys, V. (2014). Programmable RNA shredding by the type III-A CRISPR-Cas system of Streptococcus thermophilus. Mol. Cell *56*, 506–517.

Tamulaitis, G., Venclovas, Č., and Siksnys, V. (2017). Type III CRISPR-Cas Immunity: Major Differences Brushed Aside. Trends Microbiol. *25*, 49–61.

Taylor, D.W., Zhu, Y., Staals, R.H., Kornfeld, J.E., Shinkai, A., van der Oost, J., Nogales, E., and Doudna, J.A. (2015). Structural biology. Structures of the CRISPR-Cmr complex reveal mode of RNA target positioning. Science *348*, 581–585.

Wiedenheft, B., van Duijn, E., Bultema, J.B., Waghmare, S.P., Zhou, K., Barendregt, A., Westphal, W., Heck, A.J., Boekema, E.J., Dickman, M.J., and Doudna, J.A. (2011). RNA-guided complex from a bacterial immune system enhances target recognition through seed sequence interactions. Proc. Natl. Acad. Sci. USA *108*, 10092–10097.

Wu, X., Kriz, A.J., and Sharp, P.A. (2014). Target specificity of the CRISPR-Cas9 system. Quant. Biol. *2*, 59–70.

Xiao, Y., Luo, M., Dolan, A.E., Liao, M., and Ke, A. (2018). Structure basis for RNA-guided DNA degradation by Cascade and Cas3. Science *361*, eaat0839.

Xue, C., Whitis, N.R., and Sashital, D.G. (2016). Conformational Control of Cascade Interference and Priming Activities in CRISPR Immunity. Mol. Cell *64*, 826–834.

Xue, C., Zhu, Y., Zhang, X., Shin, Y.K., and Sashital, D.G. (2017). Real-Time Observation of Target Search by the CRISPR Surveillance Complex Cascade. Cell Rep. *21*, 3717–3727.

Yang, M., Peng, S., Sun, R., Lin, J., Wang, N., and Chen, C. (2018). The Conformational Dynamics of Cas9 Governing DNA Cleavage Are Revealed by Single-Molecule FRET. Cell Rep. *22*, 372–382.

Yin, J., Lin, A.J., Golan, D.E., and Walsh, C.T. (2006). Site-specific protein labeling by Sfp phosphopantetheinyl transferase. Nat. Protoc. *1*, 280–285.

Zhang, J., Rouillon, C., Kerou, M., Reeks, J., Brugger, K., Graham, S., Reimann, J., Cannone, G., Liu, H., Albers, S.V., et al. (2012). Structure and mechanism of the CMR complex for CRISPR-mediated antiviral immunity. Mol. Cell *45*, 303–313.

Zhou, Z., Cironi, P., Lin, A.J., Xu, Y., Hrvatin, S., Golan, D.E., Silver, P.A., Walsh, C.T., and Yin, J. (2007). Genetically encoded short peptide tags for orthogonal protein labeling by Sfp and AcpS phosphopantetheinyl transferases. ACS Chem. Biol. *2*, 337–346.

STAR★METHODS

KEY RESOURCES TABLE

REAGENT or RESOURCE	SOURCE	IDENTIFIER
Bacterial and Virus Strains		
Escherichia coli BL21 (DE3) Rosetta2	Merck Millipore	N/A
Staphylococcus aureus RN4220	(Kreiswirth et al., 1983)	N/A
Chemicals, Peptides, and Recombinant Proteins		
Complete-EDTA-free protease inhibitor	Sigma-Aldrich	Cat# 11873580001
RNaseOUT Recombinant ribonuclease inhibitor	Thermo Fisher Scientific	Cat# 10777019
KOD Hot Start DNA polymerase	Millipore Sigma	Cat# 71086
Gibson Assembly Master mix	New England Biolabs	Cat# E2611S
Cy3 mono-reactive NHS Ester dye	GE Healthcare	Cat# PA23001
Cy5 maleimide mono-reactive dye	GE Healthcare	Cat# PA15131
SNAP-Surface Alexa Fluor 647	New England Biolabs	Cat# S9136S
Coenzyme A trilithium salt	Sigma-Aldrich	Cat# C3019
(3-Aminopropyl)triethoxysilane	Sigma-Aldrich	Cat# A3648
Trolox	Sigma-Aldrich	Cat# 238813
Glucose oxidase	Sigma-Aldrich	Cat# G2133
Dextrose monohydrate	Sigma-Aldrich	Cat# D9559
Catalase	Sigma-Aldrich	Cat# C100
Bio-PEG-SVA and mPEG-SVA, MW5000-combo kit	Laysan Bio	Cat# 143-117, 144-136
Streptavidin	Thermo Fisher Scientific	Cat# 434302
Oligonucleotides		
See Table S1	IDT	N/A
Recombinant DNA		
pAS1	This paper	N/A
pPS22	(Samai et al., 2015)	N/A
pPS86	(Samai et al., 2015)	N/A
pSNAP-tag vector	New England Biolabs	Cat# N9181S
pLW1 (expressing Cas10-Csm complex containing SNAP-Cas10)	This paper	N/A
pLW24 (expressing Cas10-Csm complex containing SNAP-Csm5)	This paper	N/A
pLW40 (expressing Cas10-Csm complex containing SNAP-Cas10 and Csm3^{D32A})	This paper	N/A
pLW48 (expressing Cas10-Csm complex containing SNAP-Csm4)	This paper	N/A
Sfp pet29b C-terminal His Tag	Addgene	Cat# 75015
pE194	(Horinouchi and Weisblum, 1982)	N/A
pCRISPR	(Hatoum-Aslan et al., 2013)	N/A
pCRISPRΔspc	(Samai et al., 2015)	N/A
pTarget^{WT}	This paper	N/A
pTarget$^{Anti-tag}$	This paper	N/A
pTarget^{MM1-10}	This paper	N/A
pTarget$^{MM11-20}$	This paper	N/A
pTarget$^{MM26-35}$	This paper	N/A

(Continued on next page)

Continued

REAGENT or RESOURCE	SOURCE	IDENTIFIER
Software and Algorithms		
SPARTAN	(Juette et al., 2016)	https://www.scottcblanchardlab.com/software
HaMMy	(McKinney et al., 2006)	https://cplc.illinois.edu/software/
Origin	OriginLab	https://www.originlab.com
MATLAB	MathWorks	https://www.mathworks.com/products/matlab.html
PRISM	GraphPad Software	https://www.graphpad.com/scientific-software/prism/

CONTACT FOR REAGENT AND RESOURCE SHARING

Further information and request for resources and reagents should be directed to and will be fulfilled by the Lead Contact, Shixin Liu (shixinliu@rockefeller.edu).

EXPERIMENTAL MODEL AND SUBJECT DETAILS

Bacterial strains and growth conditions

Staphylococcus aureus RN4220 (Kreiswirth et al., 1983) was cultured on Bovine Heart Infusion (BHI) agar plates containing 10 μg/mL erythromycin and 10 μg/mL chloramphenicol to ensure pTarget and pCRISPR plasmid maintenance, respectively. When appropriate, anhydrotetracycline (aTc) was used at a concentration of 0.25 μg/mL to initiate transcription from the P$_{tet}$ promoter.

All expression vectors were transformed into *E. coli* BL21 (DE3) Rosetta 2 cells grown in Terrific Broth medium (Fisher Scientific) containing 100 μg/mL ampicillin and 34 μg/mL chloramphenicol at 37°C, induced at mid-log phase with 0.5 mM IPTG, and then transferred to 16°C for overnight expression.

METHOD DETAILS

Plasmid construction
Plasmid for heterologous expression of the Cas10-Csm complex in *E. coli*

pAS1 was constructed based on the plasmid pPS22 harboring the repeat-spacer array and *csm* genes encoding the Csm proteins as well as the processing enzyme Cas6 (Hatoum-Aslan et al., 2013), but modified so that it contains one single spacer targeting the *gp43* gene. To generate the Csm3^{D32A} mutation, pPS86 (Samai et al., 2015) and pAS1 were used as PCR templates with two sets of primers LW10F/R and LW11F/R (see Table S1 for sequences) respectively. The PCR products were joined by Gibson assembly and the mutation was confirmed by sequencing. To attach a SNAP-tag to the N terminus of Cas10 (or Csm5, Csm4), pSNAP-tag vector (New England Biolabs) and pAS1 were used as PCR templates with primers LW1F/R (or LW7F/R, LW34F/R) and LW2F/R (or LW6F/R, LW35F/R) respectively, and joined by Gibson assembly. To insert an Sfp-tag (GDSLSWLLRLLN) (Zhou et al., 2007) at L201 or L573 of Cas10, pAS1 was used as the PCR template with primers LW44F/10R (or LW46F/10R) and LW11F/44R (or LW11F/46R).

Plasmid for transformation assay in *Staphylococcus*

pCRISPR and pCRISPRΔspc were obtained previously (Hatoum-Aslan et al., 2013; Samai et al., 2015). To clone the pTarget^{WT} plasmid (pJTR48), a DNA fragment containing a gp43 protospacer (Jiang et al., 2016) surrounded by transcriptional terminators on either side (BBa_1006 and BBa_K864501 from http://parts.igem.org/Main_Page) was synthesized by Genewiz. This was amplified by PCR using oligos JTR234 and JTR235, and restriction cloned into pE194 (Horinouchi and Weisblum, 1982) amplified with JTR232 and JTR233 and digested with EcoRI and NotI, creating pJTR41. An NheI site was inserted upstream of the protospacer by amplifying pJTR41 with JTR248 and JTR249 by PCR, and ligating the resulting product and pJTR41, after digestion with NotI and HindIII, creating pJTR43. The aTc-inducible promoter was PCR amplified from pWJ153 (Goldberg et al., 2014) using JTR250 and JTR251, digested with NotI and EcoRI, and ligated upstream of the protospacer with digested pJTR43, creating pJTR46. To add the tetracycline repressor, pWJ153 was PCR amplified using JTR258 and JTR259. The resulting product and pJTR46 were digested with NheI and HindIII, and the resulting fragments joined by ligation.

To generate mutant pTarget plasmids, mutations in the protospacer sequence or the flanking sequences were introduced via oligonucleotide cassette-based mutagenesis. The pJTR48 plasmid was digested with two restriction enzymes, MfeI and HindIII, flanking the target gp43 sequence. The digested plasmid was then treated with Calf Intestinal Phosphatase (New England Biolabs) for 1 hour at 37°C before being purified via a standard spin column DNA cleanup procedure. Oligos (CYM339/340, CYM343/344, CYM372/373, or CYM374/375) containing the mutations (Anti-tag, MM1-10, MM11-20, or MM26-35) (see Table S1) were annealed in a thermocycler, phosphorylated with T4 Polynucleotide Kinase (New England Biolabs) for 1 hour at 37°C, and spin column purified as well. Digested plasmid and annealed oligo cassettes were then ligated with T4 DNA ligase at 16°C for 16 hours.

Protein expression and purification

pAS1 was transformed into *E. coli* BL21 (DE3) Rosetta 2 cells (Merck Millipore), grown in Terrific Broth medium (Fisher Scientific) containing 100 µg/mL ampicillin and 34 µg/mL chloramphenicol at 37°C until A_{600} reached 0.6. Cells were harvested and resuspended in a lysis buffer (50 mM Tris-HCl pH 7.5, 350 mM NaCl, 10 mM imidazole, 1 mM β-mercaptoethanol, 0.1% Triton X-100) after induction with 0.5 mM IPTG overnight at 16°C. The lysate was sonicated and the supernatant was bound to Ni-NTA agarose (QIAGEN), followed by wash flow using the lysis buffer containing 50 mM, 75 mM, and 100 mM imidazole in a stepwise manner. Cas10-Csm complexes loaded with mature crRNA were finally eluted from the Ni-NTA column with lysis buffer containing 250 mM imidazole and subsequently purified on a 1-mL Resource Q column (GE Healthcare). The peak fraction from the column was further purified by size exclusion chromatography using Superdex 200 10/300 GL (GE Healthcare) in a storage buffer (50 mM Tris-HCl pH 7.5, 150 mM NaCl, 5% glycerol). The mutant (Csm3^{D32A}), Sfp-tagged and SNAP-tagged protein complexes were purified using the same procedure.

Site-specific fluorescent labeling
Protein labeling

SNAP-tagged Cas10-Csm protein complexes were labeled at a concentration of 5 µM with 10 µM SNAP-Surface AlexaFluor647 (New England Biolabs) in 50 mM Tris-HCl pH 7.5, 150 mM NaCl, 5% glycerol, and 1 mM DTT. Sfp-tagged Cas10-Csm complexes were labeled at a concentration of 5 µM with 20 µM CoA-Cy5 and 20 µM Sfp synthase in 50 mM Tris-HCl pH 7.5, 150 mM NaCl, 1 mM DTT and 10 mM MgCl$_2$. Sfp synthase was purified on a nickel-NTA column and Cy5 was functionalized by CoA as previously described (Yin et al., 2006). The labeling mixture was incubated in dark for 2 hours at room temperature. Free dyes were removed by Superdex 200 10/300 GL.

Nucleic acid labeling

DNA and RNA oligonucleotides were purchased from IDT. RNA with a 5′ or 3′ amino modifier was dissolved in 0.1 mL of 0.5 M NaCl, flown through a Sephadex G-25 desalting column (GE Healthcare) to remove traces of ammonia, and then incubated with one pack of Cy3 mono-reactive dye (GE Healthcare) in 0.1 M NaHCO$_3$ pH 8.5 at room temperature for 2 hours. Free dyes were removed by Sephadex G-25. Labeled RNAs were subjected to ethanol precipitation and stored in TE buffer (10 mM Tris-HCl pH 8.0, 1 mM EDTA).

Bulk RNA cleavage assay

RNA cleavage reactions were performed at room temperature with 20 nM Cy3-labeled RNA and 100 nM Cas10-Csm complexes in a buffer consisting of 50 mM Tris-HCl pH 7.5, 2 mM TCEP, and 0.1 mg/mL BSA. Reactions were initiated by the addition of 10 mM MgCl$_2$. Products were collected at time intervals, quenched with 2 × loading buffer (90% formamide, 50 mM EDTA, 5% glycerol, 0.1% bromophenol blue), separated on a 12% denaturing polyacrylamide gel, and visualized on a Typhoon imager (GE Healthcare).

Bacterial transformation assay

Staphylococcus aureus RN4220 strains were first transformed with pTarget plasmids carrying the various target sequences. 100 ng of dialyzed plasmid DNA was electroporated into electrocompetent RN4220 cells using a GenePulser Xcell (BioRad) with the following parameters: 2900 V, 25 mF, 100 V, 2 mm. Electroporated strains were immediately resuspended in 500 µL of Bovine Heart Infusion (BHI) broth and grown at 37°C with shaking (220 rpm) for 1 hour. Cells were plated onto BHI agar plates containing 10 µg/mL of erythromycin and left to incubate at 37°C for 16 hours. Single colonies from the plates were picked to generate electrocompetent cells carrying the pTarget plasmids. RN4220 strains carrying the pTarget plasmids were then transformed with 100 ng of either pCRISPR or pCRISPRΔspc via the same electroporation protocol as described above. Following growth at 37°C in BHI broth for 1 hour, cells were spun down on a table-top centrifuge at 6,000 rpm for 3 min and resuspended in 1 mL of fresh BHI broth. 100 µL of the resuspended culture was plated onto BHI agar plates with 10 µg/mL of erythromycin and 10 µg/mL of chloramphenicol; another 100 µL of the same culture was plated onto BHI agar plates with 10 µg/mL of erythromycin, 10 µg/mL of chloramphenicol, and 0.25 µg/mL of anhydrotetracycline (aTc). Plates without aTc were incubated at 37°C for 24 hours, while plates with aTc were incubated for 48 hours. For each plate, the colony forming units per µg of plasmid (CFU/µg) was calculated. To quantify the efficiency of targeting for each transformed culture, the CFU in the presence of aTc was divided by that in the absence of aTc.

Single-molecule experiments
Data acquisition

Single-molecule experiments were performed at room temperature (23 ± 1°C) in an imaging buffer consisting of 50 mM Tris-HCl pH 7.5, 2 mM TCEP, 0.1 mg/mL BSA, 1 mM EDTA or 10 mM MgCl$_2$, and an oxygen scavenging system containing 1% w/v D-glucose, 1 mg/mL glucose oxidase (Sigma-Aldrich), 0.04 mg/mL catalase (Sigma-Aldrich) and 2 mM Trolox (Sigma-Aldrich). The microfluidic flow chambers were passivated with a mixture of polyethylene glycol (PEG) and biotin-PEG (Laysan Bio), incubated with 40 µL of 0.1 mg/mL streptavidin (Thermo Fisher Scientific), and washed with 100 µL of T50 (10 mM Tris-HCl pH 8.0, 50 mM NaCl). 40 µL of 500 pM biotinylated RNA was injected into the chamber and immobilized through biotin-streptavidin linkage. 40 µL of 10 nM labeled Cas10-Csm complexes was then added to the chamber and incubated for 5 min before imaging. Donor and acceptor fluorescence signals were collected on a total-internal-reflection fluorescence microscope (Olympus IX83 cellTIRF) and detected by an EMCCD camera (Andor iXon Ultra897) with a frame rate of 300 ms.

Data analysis

Fluorescence time trajectories of individual RNA molecules were extracted and analyzed by the SPARTAN software (Juette et al., 2016). The FRET efficiency (E) was calculated as $I_A/(I_D+I_A)$, where I_D and I_A represent the donor and acceptor fluorescence intensity, respectively. Dynamic FRET traces were analyzed by a hidden-Markov-model-based software HaMMy (McKinney et al., 2006). FRET contour plots and histograms were built from at least 600 molecules from multiple fields of imaging and plotted by Origin (OriginLab). Transition density plots were generated using a custom code written in MATLAB.

QUANTIFICATION AND STATISTICAL ANALYSIS

Statistical significance was determined by unpaired two-tailed Student's t tests using GraphPad Prism 7. The difference between two groups was considered statistically significant when the p value is less than 0.05 (*, $p < 0.05$; **, $p < 0.01$; ***, $p < 0.001$; ns, not significant). The number of molecules analyzed or experiments repeated is indicated in the figure legends.

DATA AND SOFTWARE AVAILABILITY

Raw data are available upon reasonable request.